Bio-Design and Manufacturing (2023) 6:390–404
https://doi.org/10.1007/s42242-022-00228-w

RESEARCH ARTICLE

Performance of novel 3D printing tools in removing coronary-artery calcification tissue

Chuhang Gao[1,2] · Zhaoju Zhu[1,2] · Zirui Huang[2,3] · Liujing Chen[1,2] · Lihong Lu[4,5] · Mingcheng Fang[4,5] · Yao Liu[6] · Bingwei He[1,2]

Received: 25 July 2022 / Accepted: 23 December 2022 / Published online: 22 February 2023

Abstract

Rotational atherectomy is an effective treatment for severe vascular calcification obstruction, and relies on high-speed grinding (typically 130,000–210,000 r/min) with miniature grinding tools to remove calcified tissue and restore blood flow. However, reports of intraoperative complications are common because of the grinding force, temperature, and debris directly acting on the body during the grinding process, which can easily cause damage to patients. In this study, three novel grinding tools were designed and fabricated and a series of experiments have been conducted to analyze the effects of tool geometry and parameters on grinding performance, that is, force, temperature, and specimen surface morphology. The results show that these tools can effectively remove simulated calcified tissue and that they have two motions, rotation and revolution, in the tube. At higher rotational speeds, grinding force and temperature increase noticeably, while the amount of debris decreases significantly. In addition, by observing the surface morphology of the specimens, we concluded that the material removal rate per unit time is influenced by both rotational speed and tool geometry, and that high rotational speed and a rough tool surface can improve the material removal rate efficiently.

✉ Zhaoju Zhu
zhaojuz@fzu.edu.cn

1 College of Mechanical Engineering and Automation, Fuzhou University, Fuzhou 350001, China

2 Fujian Engineering Research Center of Joint Intelligent Medical Engineering, Fuzhou 350001, China

3 Maynooth International Engineering College, Fuzhou University, Fuzhou 350001, China

4 Shengli Clinical Medical College of Fujian Medical University, Fuzhou 350001, China

5 Department of Cardiology, Fujian Provincial Hospital, Fuzhou 350001, China

6 Advanced Manufacturing Technology of Shanxi Key Lab, North University, Taiyuan 030051, China

Graphic abstract

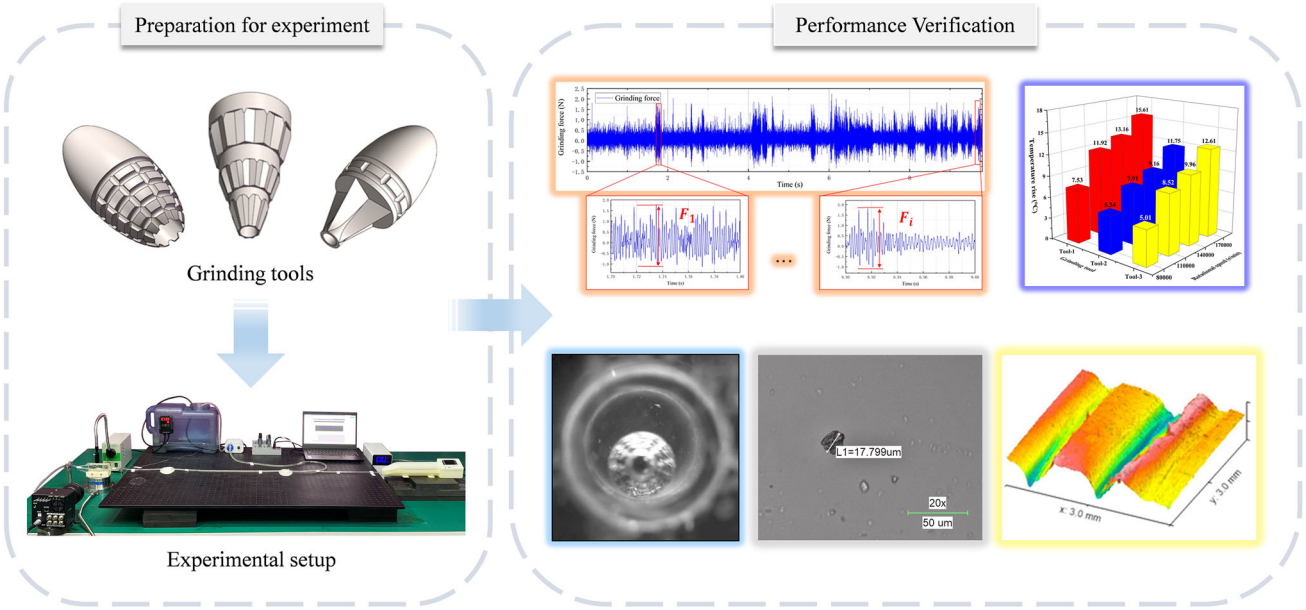

Keywords Rotational atherectomy · Grinding tool · Grinding performance · Parameter analysis

Introduction

Atherosclerosis is a common cardiovascular disease with a high prevalence in hypertensive and hyperlipidemic populations, and is a major cause of coronary heart disease, cerebral infarction, and peripheral vascular disease. The formation of calcified tissue and blockage of blood vessels are the main manifestations of atherosclerosis. These atheromas are a kind of hard lump formed by the deposition of fat, calcium carbonate, and other substances on the inner wall of blood vessels. Starting from soft fatty spots, there is gradual thickening and hardening that finally forms calcified tissue with a hard texture and highly similar microstructure to bone, accompanied by inflammation and apoptosis [1–4]. Percutaneous coronary intervention (PCI) is a common treatment for calcified vascular stenosis; it is a catheter-based minimally invasive procedure to remove the plaque, and commonly used methods include balloon angioplasty, coronary stenting, and rotational atherectomy (RA) [5–7]. When the vessel is heavily obstructed by calcification, the balloon and stent are constrained by the calcified tissue in the vessel and cannot be effectively deployed, and when the calcified lesion occurs in a vessel with a large curvature the balloon and stent cannot adapt to the shape of the vessel. In these cases, RA becomes the most effective treatment [8, 9].

RA combines the techniques of grinding and biological tissue removal to achieve effective removal of calcified tissue. Clinically, the RA miniature grinding tool is inserted into the body through the femoral/radial artery and travels along the arterial vessels to the diseased area [10]. It grinds the calcified tissue at 130,000–210,000 r/min (driven by the drive shaft), resulting in tiny particles of calcified tissue that can be engulfed and absorbed by the liver, spleen, lungs, and endothelial phagocytes, ultimately modifying the calcified tissue and enlarging the vascular lumen [11, 12], as shown in Fig. 1. The grinding tool used in RA is an ellipsoidal metal workpiece with a diameter of 1.25–2.5 mm and the surface is coated with diamond abrasive. The appropriate size can be selected during the operation according to the lumen size. RA has been used clinically for more than 30 years, but there is a potential for major adverse cardiovascular events due to the entry of the abrasive head as a foreign body and its high-speed action [13]. Common

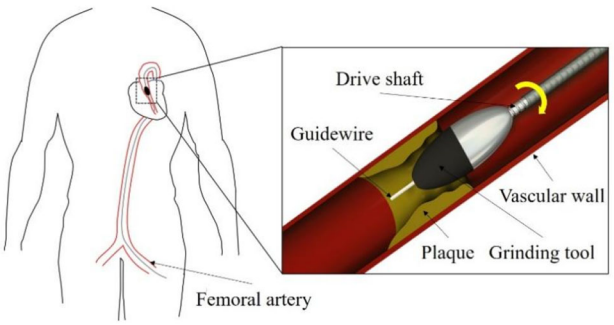

Fig. 1 Schematic of rotational atherectomy (RA)

surgical complications include vascular dissection, slow/no reflow, distal vessel obstruction, and myocardial infarction [14, 15]. The human operator and stability of the RA device also directly affect the outcome of RA. Vascular dissection is mainly caused by excessive grinding force, which tears the intima and causes blood to flow from the fissure to the intima-media union surface [16]. If the grinding debris is too large to be absorbed and metabolized by the body, it can block the capillary blood, causing ineffective blood circulation and eventually leading to the slow/no-reflow phenomenon [17, 18]. Meanwhile, blood cells are prone to thrombosis when heated, and grinding temperature is an important factor in potential thrombosis. If thrombosis cannot be quickly removed, it causes myocardial infarction and other malignant cardiovascular events, endangering patients' lives [19]. In addition, there are some phenomena such as tool off-loading, particle dropping, and tool sticking which can occur [20–22], besides some hidden dangers in the RA device itself.

As in other biological tissue-removal operations, grinding may cause unnecessary damage to normal body tissues. In view of this problem, more and more scholars are combining engineering knowledge with medical applications. Innovative surgical tools have been proposed to optimize the therapeutic effect and reduce the chance of injury. Nakao et al. [23] used a punch to prepare a 5-μm projection on the tool as a micro-edge and ground an egg shell (on the egg) in water at 150,000 r/min. The grinding tool conformed to the "differential cutting" principle, effectively removing the egg shell without damaging the egg white. Lee et al. [24] used laser-engraving technology to prepare micro-nicks on the grinding tool, and used a hydroxyapatite/polylactic acid composite material as a substitute for calcified tissue to analyze the grinding force and the size of debris; they verified the feasibility of the grinding tool. Lyu et al. [25] coated the drive shaft with diamond abrasive particles and ground a gypsum model for 10 s. They found that the diameter of the model cavity expanded from 2 to 3.53 mm, proving that the grinding tool had sufficient grinding efficiency. Mizutani et al. [26] proposed a surgical tool coated with titanium dioxide to solve the problem of excessive bone-grinding heat in orthopedic surgery. Their experiments showed that the tool effectively inhibited an increase in grinding temperature. Luo et al. [27] developed a hollow Kirschner wire for bone-drilling experiments, and the results showed that compared with traditional Kirschner wire, the temperature, thrust, and torque generated by the new Kirschner wire were reduced significantly, which reduced the probability of bone overheating and necrosis in orthopedic surgery. Liu et al. [28] made different grooves in the front of the Kirschner wire, and found that grooves helped to remove debris, reduce heat generation, and optimize the effect of bone drilling.

The above studies showed that the idea of combining engineering and medicine to improve medical devices can play a positive role in increasing the efficiency of devices and improving treatment results. The main grinding devices currently in use for RA are the RA (Rotablator™) manufactured by Boston Scientific and the OA (Diamondback 360®) manufactured by Cardiovascular System Inc. Both of them use tiny tools with diamond abrasive grains plated on the surface, which mainly rely on the grinding process to remove calcified tissue during RA. They have problems such as low efficiency and clogging of blood vessels from shedding of abrasive grains. Compared with the standard grinding tools, the structure of the novel grinding tools tested in this study integrated engineering design ideas, and the tools were prepared by titanium alloy powder three-dimensional (3D) printing molding technology.

This paper focuses on improvement strategies for tools used in RA, and in it we propose three novel grinding tools. We first introduce the structural design and parameters of the tools, then describe our experimental platform for verifying performance, and finally discuss the grinding force, temperature, and debris morphology observed during the grinding process.

Materials and methods

The experimental setup consisted of a grinding device, temperature-measurement system, force-measurement system, high-speed camera, and simulated blood-delivery system, as shown in Fig. 2.

The grinding device comprised a drive unit, a grinding tool, and a drive-shaft assembly. The drive unit had a direct current (DC) brushless motor and a speed-increasing gear train; the grinding tools were special microtools we designed, the specific parameters of which are described in the next subsection. The total length of the nickel-titanium alloy medical flexible drive shaft was 135 cm, and the outside was covered with a protective sheath of Teflon material. The grinding tool was mounted on the end of the drive shaft. We used deionized water as simulated blood and kept it in a container at a constant temperature (the human core temperature of 37 °C). For the experiment, it was drawn through a precision peristaltic pump into a simulated blood vessel (a clear, flexible polyvinyl chloride (PVC) tube).

Grinding-tool design

Tool-1 was a modification of the Rotablator device, with interlaced semicircular grooves added to the front part of the tool, with a groove cross-sectional diameter of 0.4 mm, an average depth of (0.2±0.05) mm, an average interval of (0.6±0.05) mm between grooves arranged along the circumference, and a maximum interval of (1±0.05) mm between grooves arranged along the axial direction. The sharp edges

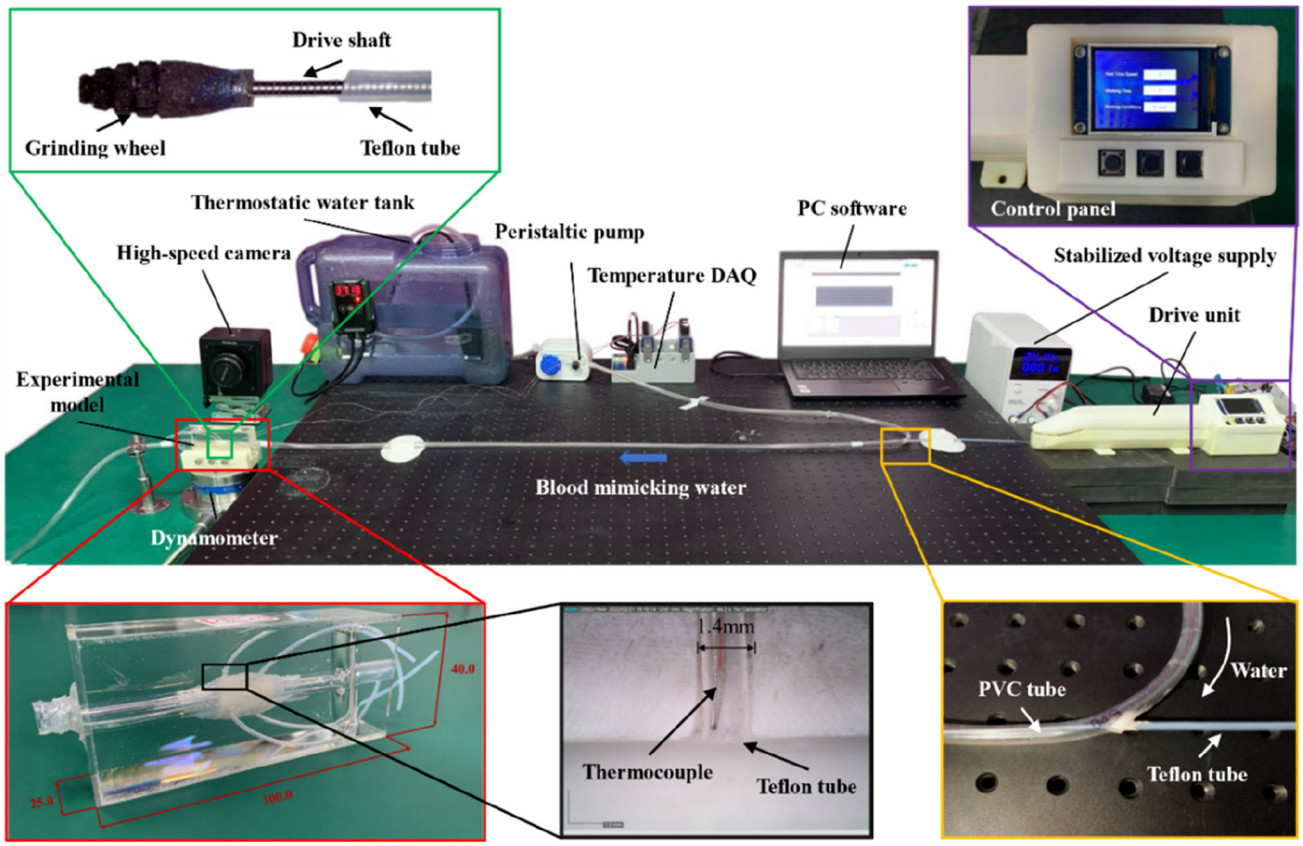

Fig. 2 Experimental setup (DAQ: data acquisition system; PC: personal computer; PVC: polyvinyl chloride)

of the grooves enabled the tool to cut as well as grind, increasing the rate of material removal.

Tool-2 had three graded steps with diameters of 4.5, 3.3, and 2.2 mm, respectively, and micro-edges with a top angle of 120° arranged around the outer circumference of the bevels of each grade. During the grinding process, the single feed was usually small, and the tool had to be slowly and continuously advanced. As the calcified tissue was continuously removed and the inner diameter increased, the stepped shape of the tool was able to adapt well to the trend of gradual expansion of the inner diameter of the calcified tissue, ensuring that the calcified tissue could always be effectively ground, reducing the number of tool changes, and shortening the surgical operation time.

Tool-3 was designed with blades placed 90° apart circumferentially, and grooves arranged in the middle of the grinding tool to increase the surface roughness (similar to Tool-1). The multiple edges of the design effectively improved the removal efficiency of grinding, and the grinding area in the middle of the tool ensured the removal efficiency of the material while producing a smoother inner surface that gave better access to subsequent surgical instruments.

In order to reduce weight, the inside of the tools was hollow and only the support material was retained. The specific parameters of each tool are given in Table 1.

Experimental materials and equipment

For this study, we designed three novel grinding tools and fabricated them with a metal 3D printer (ProX DMP 320 by 3D Systems). The tools can be classified into groove type (Tool-1), stepped type (Tool-2), and multi-blade type (Tool-3) according to their shape characteristics, and the material was Ti6Al4V.

Fresh bovine compact bone was chosen as the test material because calcification of coronary arteries is one of the manifestations of coronary atherosclerosis, and heavily calcified tissue shows a microstructure similar to that of bone. It has been shown that the mechanical properties and composition of human calcified tissue and bovine compact bone are very similar [29–31]. The bone was processed into a circular bone block with an inner diameter of 5 mm and a smooth inner surface using core drills, twist drills, and boring tools; the roughness of the inner surface of the processed bone was $R_a \leq 0.22$ μm. In order to prevent moisture loss from the compact bone, we refrigerated it at −8 °C. Soft PVC tube was

Table 1 Grinding-tool parameters and structure

	Tool-1	Tool-2	Tool-3
Diameter (mm)	4.5±0.02	4.5±0.02	4.5±0.02
Length (mm)	8.62	8.34	9.03
Weight (g)	0.4193	0.2205	0.3500
3D model	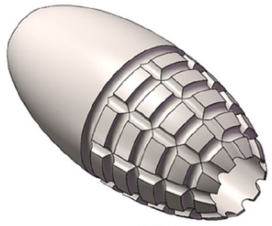	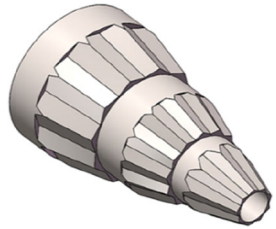	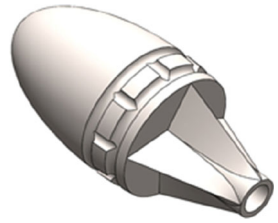
Structure diagram	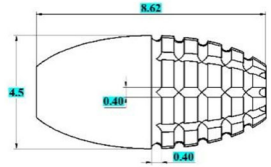	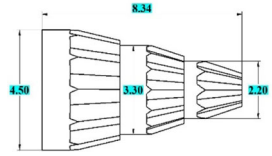	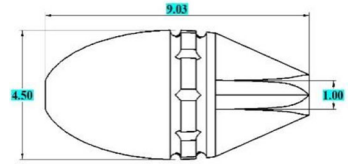
Figure			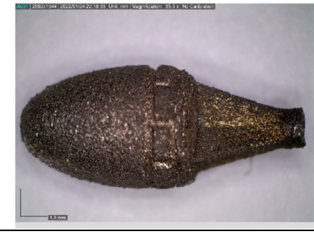

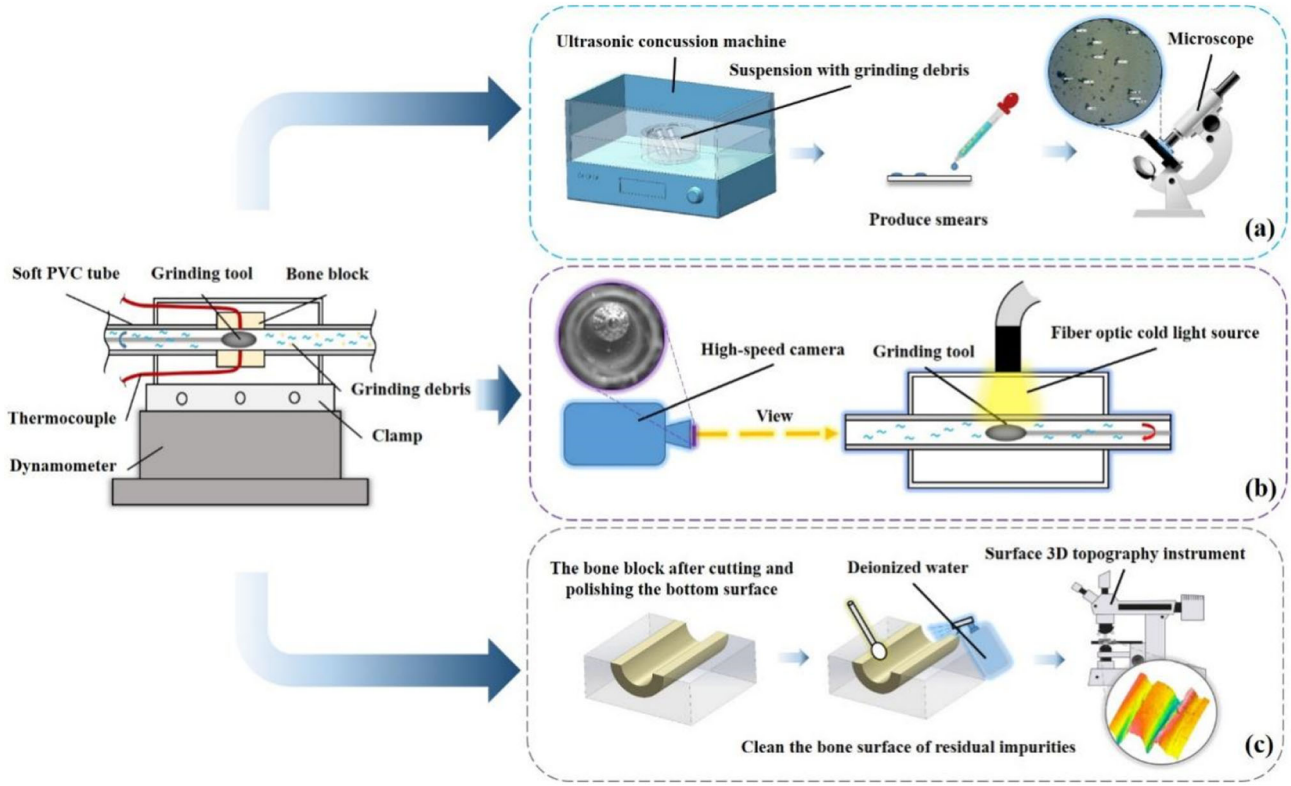

Fig. 3 Schematic diagram of experimental data acquisition: **a** suspension processing and debris-morphology measurement; **b** grinding-tool trajectory measurement; **c** 3D morphometry measurement of the inner surface of the bone (PVC: polyvinyl chloride)

used as the simulated blood vessel, and the deionized water stored in the constant temperature tank (at 37 °C) was fed into the tube, after the peristaltic pump was pressurized, as the simulated blood.

To ensure accurate and reliable temperature data, a pair of thermocouples (Model 5-TC-TT-K-36 by Omega) fixed along the circumferential direction were prearranged in the calcified tissue-encapsulation model. The head nodes of the two thermocouples were flush with the inner surface of the calcified tissue, and the temperature feedback difference between the two thermocouples was checked before measurement (less than or equal to 0.1 °C qualified) and cold-end compensation was performed. The temperature sampling rate was set to 100 Hz, and the temperature data were transmitted to the upper computer via a temperature-acquisition card (Model 9219 by National Instruments). The grinding-force data were measured with a high-precision piezoelectric-force-measuring instrument (Model 9257 by Kistler), the calcified tissue encapsulation model was fixed above the force-measuring instrument by a special fixture, and the grinding-force sampling rate was set to 10,000 Hz. We used a high-speed camera (Model FASTCAM Mini AX200 by Phantom) to record the trajectory of the grinding tool at 6400 frames/s. To improve the image quality of the camera, we placed a fiber-optic light source (Model GP601L by GAOPIN) above the encapsulation model to increase the light intake of the camera lens. After completing the grinding operation, we cut the calcified tissue-encapsulation model in half and polished it flat, in addition to removing the impurities on the inner surface of the calcified tissue using an ultrasonic concussion machine. We measured the inner surface morphology and grinding depth using a surface 3D morphology measuring system (Model Micromeasure2 by STIL). The debris suspension was collected and pretreated for 10 min using an ultrasonic concussion machine to prevent micro abrasive chips from flocculating in the water and reducing measurement accuracy. The experimental data acquisition process is shown in Fig. 3.

Experimental design

Four grinding speeds (80,000, 110,000, 140,000, and 170,000 r/min) were used for the experiments. During the experiments, we acquired grinding force and temperature and recorded the trajectory of the grinding tool; and we controlled the simulated blood-flow rate to approximate the human coronary blood-flow rate of 30 mL/min. After the experiments, we collected the debris suspension for morphology measurement, and also measured the internal surface morphology and grinding depth. To ensure the accuracy of the

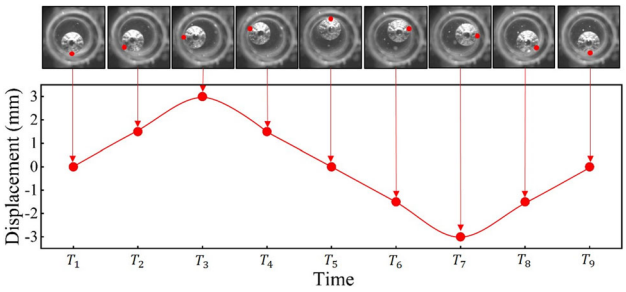

Fig. 4 Grinding-tool motion. The red dots represent the points of contact between the collision of the tool and the inner wall of the tube

experimental data, each group of experiments was repeated five times independently, and the average value of the five measurements was taken as the experimental result.

Results and discussion

Grinding-tool motion

The motion of the tools was recorded by a high-speed camera arranged in front of the platform. The frame rate of the camera was set to 6400 frames/s, and the motion was recorded after the tool had accelerated to the specified speed. We recorded images of the stable grinding section for analysis. Figure 4 gives the curve of the position of the tool in one cycle with time, as well as a picture of its corresponding radial position. A complete revolution cycle was divided into nine time points. From the figure, it can be seen that the grinding tool rotated in the lumen while also rotating around the vessel wall and bouncing slightly against the lumen wall in the process. When the rotational speed was constant, the orbital periods of the tools were very similar, so we were able to obtain the rotation frequency by calculating the rotation time of each tool at different rotational speeds.

The orbital frequencies of Tool-1, Tool-2, and Tool-3 at 80,000, 110,000, 140,000, and 170,000 r/min and the corresponding standard deviations of the data are given in Table 2. It is apparent from the table that the orbital frequency increased with the increase of rotational speed. Taking the measurement results for Tool-1 as an example, at four grinding speeds, the orbital frequency was 198.2, 328.2, 423.9, and 484.8 Hz. The orbital frequency rose significantly as rotational speed increased, and when the rotational speed increased from 80,000 to 170,000 r/min, the orbital frequency of Tool-1 increased by 144.6%. We took the mean value from five independent experiments in the same group as the measurement result, and calculated the standard deviation of the five experiments to be less than 5% of the mean value, which demonstrated the reproducibility and consistency of the measurement results. Fluctuations in orbital frequency may be caused by small changes in the front-end load, resulting in some fluctuations in rotational speed.

Table 2 Grinding-tool orbiting frequency at four rotational speeds

Grinding tool	Rotational speed (r/min)	Mean (Hz)	Standard deviation (Hz)
Tool-1	80,000	198.2	8.74
	110,000	328.2	10.27
	140,000	423.9	14.33
	170,000	484.8	16.67
Tool-2	80,000	139.1	5.02
	110,000	199.7	9.21
	140,000	301.9	12.10
	170,000	410.3	17.51
Tool-3	80,000	228.6	10.26
	110,000	309.2	5.46
	140,000	353.6	17.54
	170,000	507.9	21.43

Grinding forces

Previous studies have demonstrated an association between excessive grinding force and surgical complications such as vascular dissection and tunica intima injury; therefore, analysis of grinding force was one of our concerns in this study. To avoid the influence of gravity on measurement results, we selected the F_y grinding-force signal for analysis, and used DynoWare software to low-pass filter the grinding-force signal to reduce the influence of environmental interference.

To investigate the differences in grinding forces of the three tools at different rotational speeds, we conducted a total of 12 groups of grinding experiments. The data were processed by intercepting the grinding-force waveform, calculating the peak-to-peak values of each waveform and accumulating them, and finally calculating the average value of the grinding force according to the actual number of selected cycles from the grinding-force results of the group of experiments. The measurement results were obtained by averaging the results of five independent experiments, and the original and local waveforms of the grinding force were selected, as shown in Fig. 5.

The equation used to calculate the mean value of the grinding force was

$$\overline{F} = \sum_{i=1}^{n} \frac{F_i}{2n},$$

where n is the number of selected grinding-force waveforms, and F_i is the peak-to-peak value of each waveform.

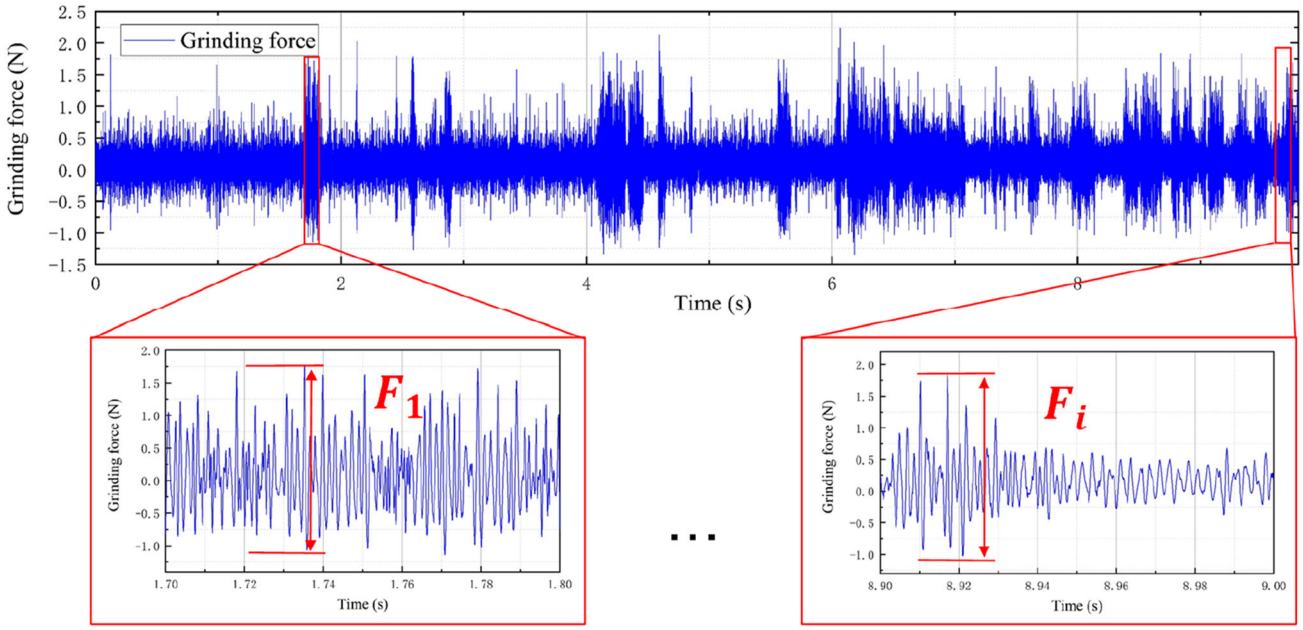

Fig. 5 Waveform of grinding force and partial signal, enlarged

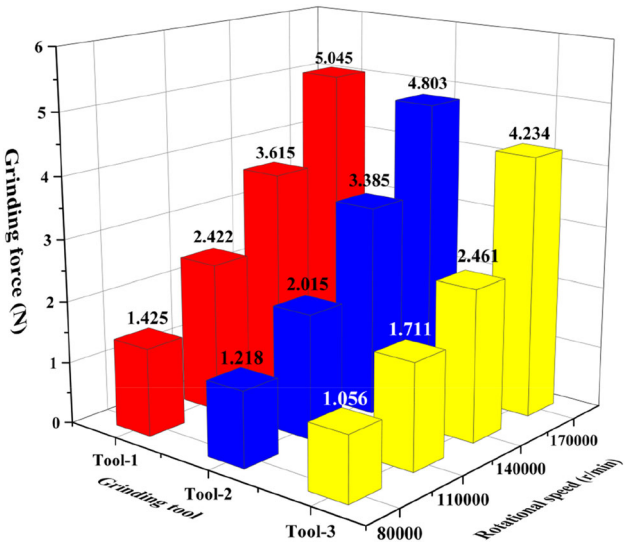

Fig. 6 Effect of different speeds on grinding force

The measurement data are shown in Fig. 6, from which it is easy to see that the grinding forces of Tool-1, Tool-2, and Tool-3 showed gradual increase from 80,000 to 170,000 r/min. The grinding force of Tool-1 increased from 1.425 to 5.045 N, that of Tool-2 increased from 1.218 to 4.803 N, and that of Tool-3 increased from 1.056 to 4.234 N. Thus, the increases were 254%, 294%, and 301%, respectively. The trend of increasing grinding force with increasing rotational speed coincides with the trend of increasing orbital frequency with increasing rotational speed described in the previous subsection. This is because the main source of grinding force was the collision force of the tool against the inner wall of the bone. At faster rotational speeds, the tool rotated around the inner wall at a higher orbital frequency, and the speed of bouncing and collision increased simultaneously, which meant that the tool hit the inner wall with higher acceleration. The collision force tends to increase in this process, which eventually leads to an increase in grinding force.

Further analysis showed that with other experimental conditions kept constant, the higher the rotational speed, the faster the orbital frequency of the tool. The tools then collided with the inner wall of the bone at a faster movement speed, resulting in the tool head invading the bone block more deeply during contact and an increase in grinding-arc length. This in turn increased the contact area between the tool and the bone, along with the number of effective abrasive grains involved in grinding. The overall effect of these combined factors was greater grinding force. As can be seen from Fig. 6, the grinding forces corresponding to the three tools at the same rotational speed are also significantly different. For example, the grinding forces measured at 170,000 r/min were 5.045, 4.803, and 4.234 N, respectively, for Tool-1, Tool-2, and Tool-3. It is evident that the grinding forces of Tool-1 are the largest among the three tools. The main reason for this phenomenon may be the difference in the quality and structure of the tools, as explained in the next paragraph.

Based on the tool parameters given in Table 1, the masses of Tool-1, Tool-2, and Tool-3 are 0.4193, 0.2205, and 0.3500 g, respectively. Tool-1 has the largest mass of the three and had regularly arranged grooves on its surface. The larger mass means that the grinding head has more kinetic

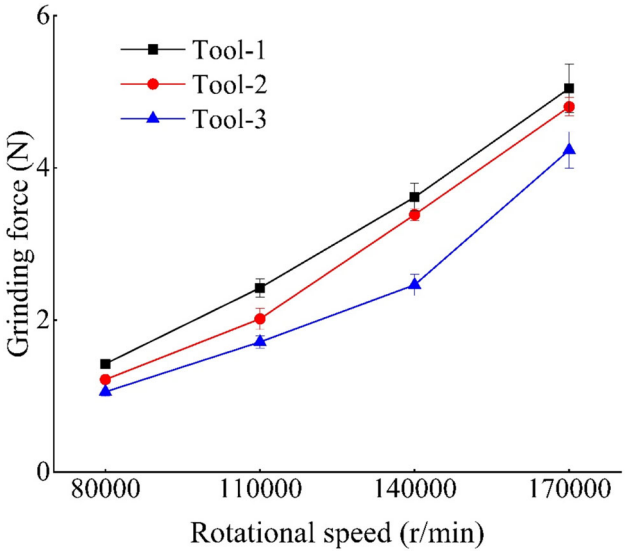

Fig. 7 Effect of different speeds on grinding force

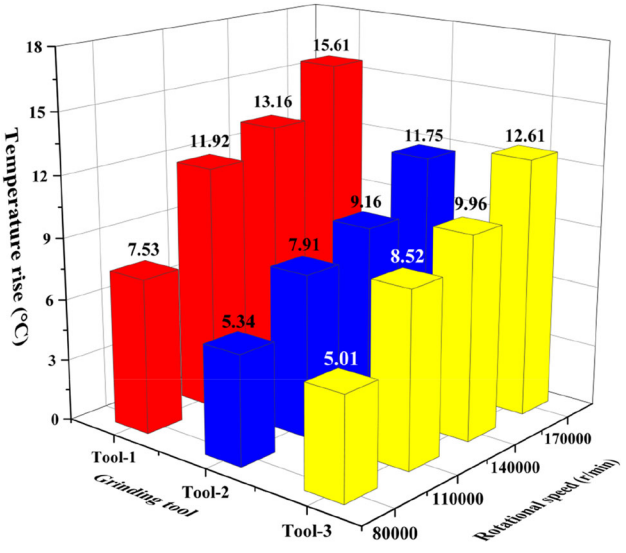

Fig. 8 Effect of different rotational speeds on grinding temperature

energy during impact and the edge of the groove acts like a blade to scrape against the wall of the bone, so its grinding efficiency is most pronounced and its grinding force is higher, as discussed in "Internal surface morphology of the specimen" section. Tool-2 has the smallest mass among the three tools due to its internal hollowing, but its radial dimension is stepped, so that the tool can effectively fit into the inner surface of the bone during grinding, ensuring that the tool has multiple micro-edges for effective grinding. The advantage of the stepped type is that the contact area between the tool and the bone is larger, so the corresponding grinding force of Tool-2 is still similar to that of Tool-1 even if the workpiece mass is significantly smaller. The surface of Tool-3 is divided into a grinding area composed of grooves and a cutting area composed of micro-edges. The micro-edges in the front are arranged 90° apart along the circumference, and at most one micro-edge is in contact with the inner wall of the bone at a time. The contact area of Tool-3 is the smallest of the three workpieces, so its grinding force is correspondingly the smallest. The measured grinding force of each experimental group is given in Fig. 7.

Grinding-temperature analysis

RA is a typical internal grinding operation in which the tool grinds the calcified tissue and thus generates heat in the grinding area. Heat acts on the human body directly, causing the risk of thrombus and tissue thermal damage, so we analyzed heat production in the process of RA as a focus of this study.

Before the experiment, the pre-heated, treated simulated blood was passed into the PVC tube, and after it was circulating stably, the temperature inside the calcified tissue cavity was measured using thermocouples to ensure temperature stability (the temperature feedback difference between thermocouples was <0.1 °C). The maximum difference between the temperature before and after the experiment was recorded as the temperature increase, and each experiment was repeated five times independently. The average value of the temperature data measured in the five experiments is shown in Fig. 8.

A noticeable temperature increase was observed in the grinding area, and the temperature increased with the increase of the rotational speed. As can be seen from Fig. 8, when the rotational speed increased from 80,000 to 170,000 r/min, the temperatures of Tool-1, Tool-2, and Tool-3 increased from 7.53, 5.34, and 5.01 °C to 15.61, 11.75, and 12.61 °C, respectively (107.3%, 120.03%, and 151.7%). This is because the tools collided with the bone at a higher speed, increasing grinding force, which in turn increased the friction between the tool and the inner wall of bone and eventually led to a higher temperature. On the other hand, at faster rotational speeds, the area of the tool involved in grinding increased per unit time, resulting in increased friction and more heat.

Taking the temperature-rise measurement at 170,000 r/min as an example, the temperature rise for Tool-1, Tool-2, and Tool-3 was 15.61, 11.75, and 12.61 °C, respectively. The heat generated by Tool-1 was significantly greater than that generated by the other two. This may be due to the large mass of Tool-1, which has higher kinetic energy at the same rotational speed. When colliding with the inner surface of the bone, a greater grinding force is generated, which in turn causes an increase in the grinding depth, the grinding contact arc length, and the cutting deformation force. The grinding load increases accordingly, increasing grinding energy; the heat flux in the grinding area increases, and the grinding temperature rises significantly. On the

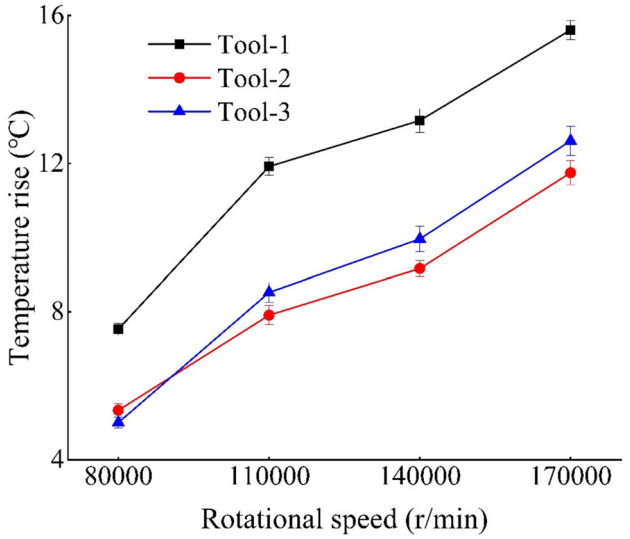

Fig. 9 Effect of different speeds on grinding temperature

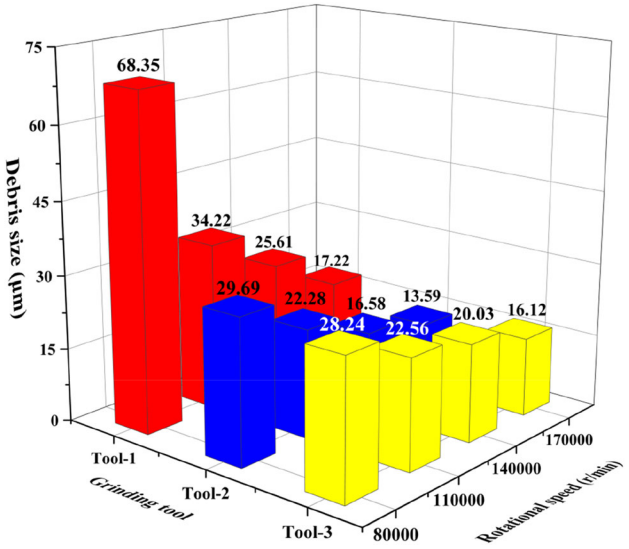

Fig. 10 Effect of different rotational speeds on debris size

other hand, the front section of Tool-1 has several grooves with sharp edges, which play a role similar to the "cutting edge" in the grinding process. This improves the efficiency of material removal and also intensifies the friction between the tool and the inner wall of the bone, so the heat generation is more evident. The measured temperature rise of each experimental group is given in Fig. 9.

Debris-morphology analysis

Ideally, calcified tissue would be ground into tiny debris that would enter the bloodstream and eventually be absorbed by the body. However, some of the large-diameter debris fails to pass through the capillaries, thus blocking the distal vessels of the heart and causing poor blood flow; this can cause serious cardiovascular events such as myocardial infarction. Therefore, we carefully analyzed the debris generated during the grinding process. The debris suspension was collected during the experiment, and some of the liquid was extracted into test tubes and shaken in water for 15 min using an ultrasonic cleaner to prevent excessively small debris from flocculating in the water, which would affect the accuracy of measurement. Each group of experiments was independently repeated five times, with 20 batches of debris sampled and debris size recorded each time. Experimental measurement data are shown in Fig. 10.

From Fig. 10, it is easy to see that the debris size decreased with increasing rotational speed. The debris size was reduced from 68.35, 29.69, and 28.24 μm to 17.22, 13.59, and 16.12 μm, respectively (for Tool-1, Tool-2, and Tool-3) when rotational speed was increased from 80,000 to 170,000 r/min, a significant reduction. The reason for this phenomenon may be that as grinding speed increases, collision force increases, which leads to deeper grinding depth and higher impact on the debris. Thus more debris is split into smaller particles and the size of the debris is considerably reduced.

Table 3 Distribution of debris size at 170,000 r/min

Grinding tool	20% of debris (μm)	50% of debris (μm)	90% of debris (μm)
Tool-1	≤11.52	≤17.22	≤20.62
Tool-2	≤13.04	≤15.64	≤23.45
Tool-3	≤10.31	≤13.42	≤19.61

Table 3 shows the debris size distribution at 170,000 r/min, given three size-parameter points for the particle size; i.e., the maximum debris size for a given volume-percentage condition is calculated. One can see from the table that when the rotational speed reaches the same speed as the RA operation (170,000 r/min), the debris can meet the safety size index (size less than 30 μm) [32]. The measured results are slightly greater than those obtained experimentally by Ahn et al. [33] on cadaveric calcified tissue (90% less than 20 μm), and the source of the experimental error may be the difference in material properties between bovine compact bone and human calcified tissue.

An image of debris produced at a rotational speed of 170,000 r/min is shown in Fig. 11.

Internal surface morphology of the specimen

Grinding depth visually reflects the degree of tool penetration into the bone, and analysis of the grinding depth can determine the material-removal efficiency of different tools. In this

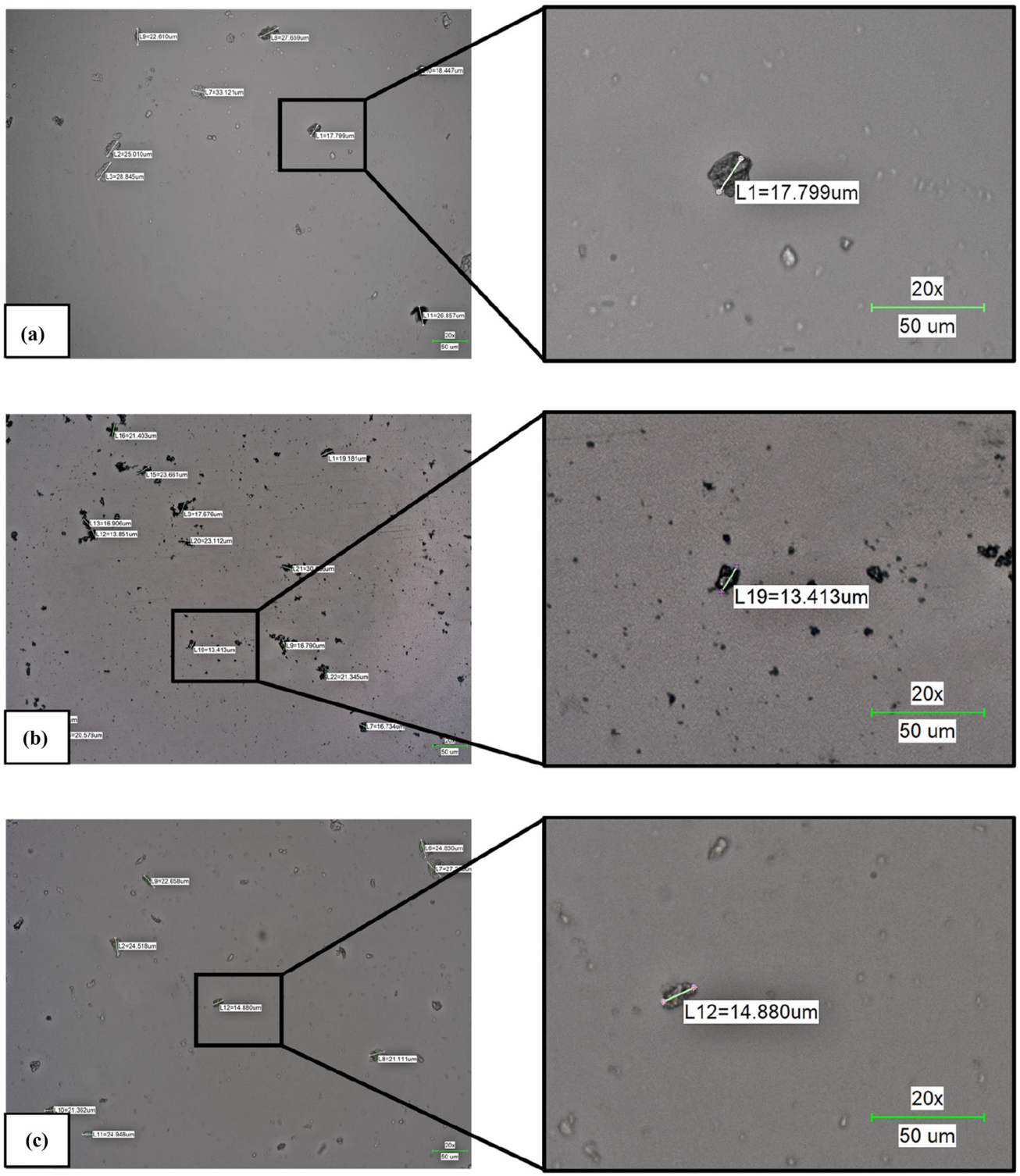

Fig. 11 Debris morphology: **a** debris produced by Tool-1; **b** debris produced by Tool-2; **c** debris produced by Tool-3

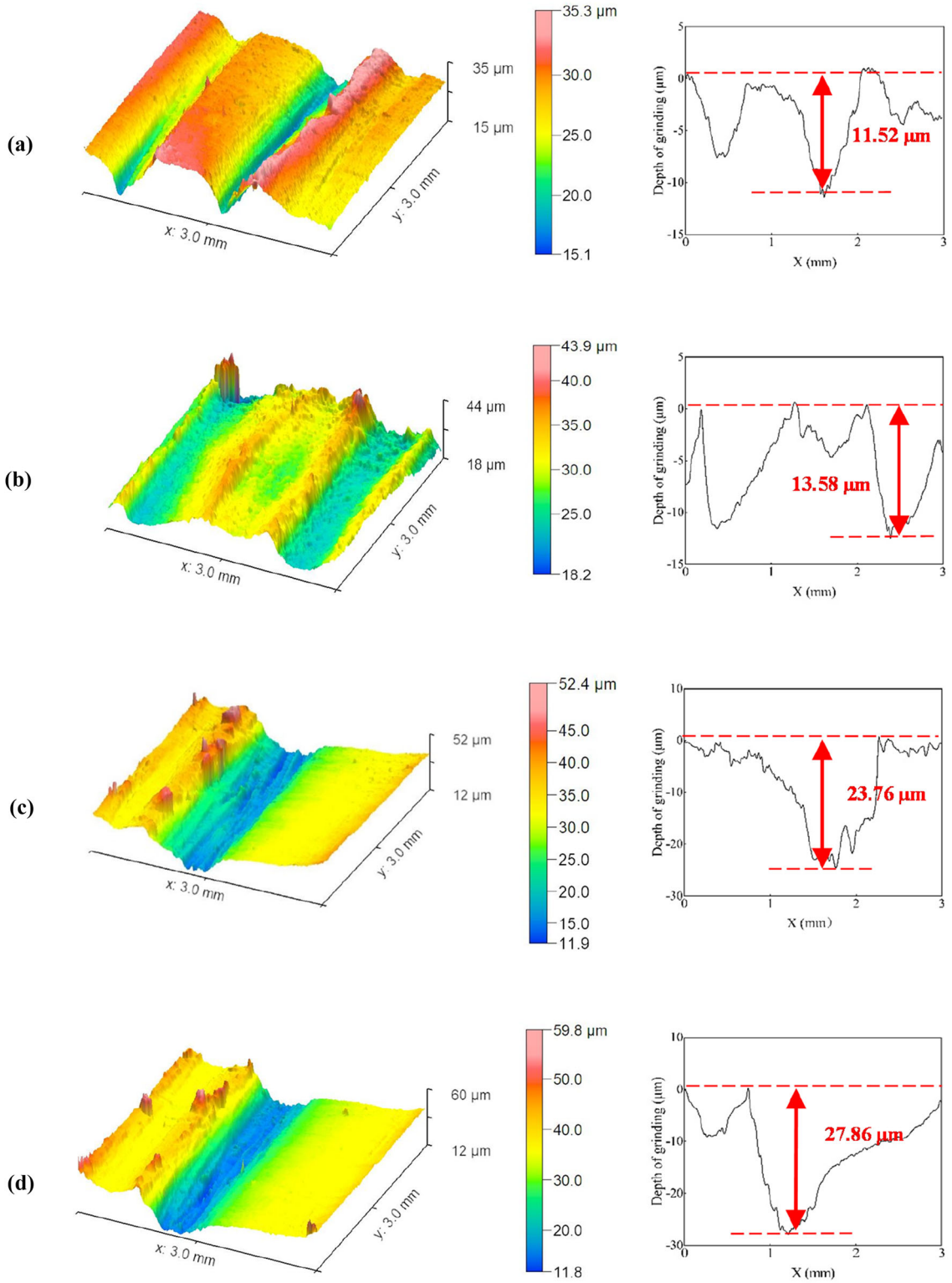

Fig. 12 The internal surface morphology and grinding depth of a sample ground with Tool-1: **a** rotational speed of 80,000 r/min; **b** rotational speed of 110,000 r/min; **c** rotational speed of 140,000 r/min; **d** rotational speed of 170,000 r/min

Table 4 Depth of grinding for Tool-1

Rotational speed (r/min)	Average depth (μm)	Maximum depth (μm)	Standard deviation (μm)
80,000	11.28	11.52	0.49
110,000	13.44	13.58	0.62
140,000	23.19	23.76	0.66
170,000	27.02	27.86	1.27

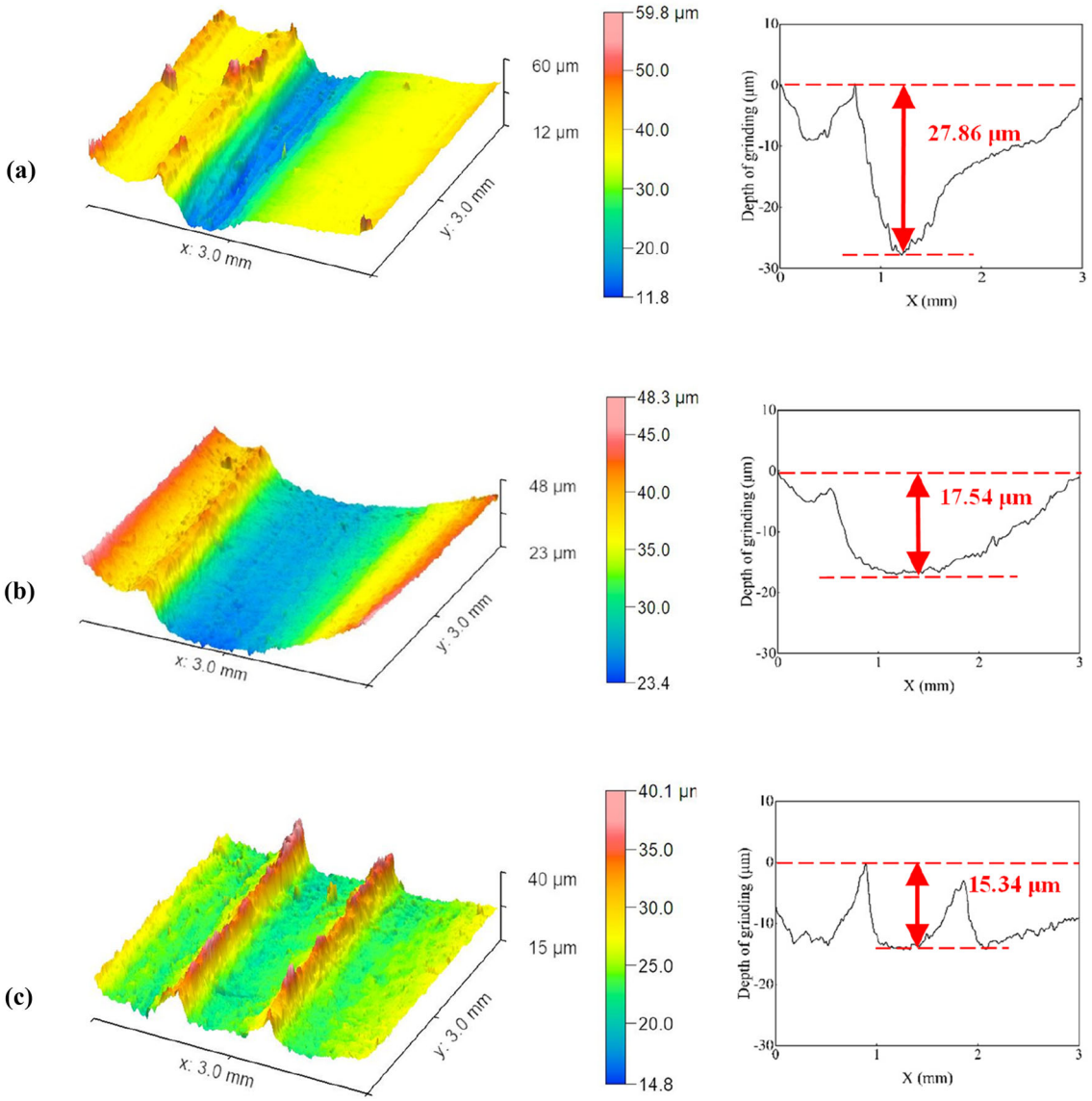

Fig. 13 Internal surface morphology and grinding depth of samples at constant rotational speed for **a** Tool-1, **b** Tool-2, and **c** Tool-3

study, we recorded the grinding depth data with a surface-topography instrument after ultrasonic cleaning of the bone. Figure 12 shows the 3D images of the internal surface morphology and grinding depth of the bone after grinding by Tool-1 at different grinding speeds.

Figure 12 illustrates that the grinding depths of Tool-1 at rotational speeds of 80,000, 110,000, 140,000, and 170,000 r/min were 11.52, 13.58, 23.76, and 27.86 μm, respectively, and the grinding depth increased with higher rotational speed. This is because as the grinding speed increases, the tool rotates and bounces at a higher speed in the cavity, resulting in an increase in collision forces and ultimately an increase in the depth of tool penetration into the material. Based on the principle of grinding, it can be

easily concluded that when the grinding speed increases, the grinding depth and effective grinding area of the tool increase, generating more grinding force and more intense heat exchange in the grinding area. This also confirms our conclusions in "Grinding forces" and "Grinding-temperature analysis" sections, that grinding force and temperature increase with grinding speed. To ensure the accuracy and reproducibility of the measurement data, five independent replicate experiments were conducted (see Table 4).

Figure 13 shows the grinding-depth measurements of the three tools and the morphology of the inner surface of the bone at a constant spin speed of 170,000 r/min. Figure 13 shows that the grinding depths of Tool-1, Tool-2, and Tool-3 at 170,000 r/min were 27.86, 17.54, and 15.34 μm, respectively. The experimental grinding depth value for Tool-1 was significantly larger, which may be due to the large mass and rough surface of Tool-1; the grinding effect was obvious in the grinding process. Observing Fig. 13b, it can be seen that curved craters appeared on the inner surface of the specimen after Tool-2 grinding, due to the stepped profile of Tool-2. Tool-2 has a head with a small diameter, creating a "drilling" effect, and a tail with a large diameter, which grinds. The combined action creates arc-shaped pits in the grinding area, effectively expanding the lumen of the bone with axial feeding.

Conclusions

In this study, we designed and fabricated three novel types of grinding tools and built a matching experimental platform. The feasibility of the tools was analyzed by five performance indicators: tool kinematics, grinding force, temperature, debris, and specimen internal surface morphology. We assessed the correlation between the five performance indicators, and looked at the influence of grinding speed and tool parameters on grinding results. The average relative error of each group of experiments is within 5%, which fully proves the accuracy and reproducibility of the experiments. The following conclusions can be drawn:

1. When a grinding tool rotates at high speed in a simulated vascular cavity, two aspects of motion can be discerned: tool rotation and revolution around the tube. The movement frequency of the tool's rotation around the tube increases with grinding speed.
2. Grinding force, temperature, and grinding depth increase with the increase of grinding speed but are also affected by the tool parameters. The larger the mass and the rougher the surface of the tool, the greater the grinding force and temperature during the grinding process.
3. At higher rotational speeds, debris size tends to decrease; at the same speed, the larger the mass of the tool, the larger the debris.

Acknowledgements This work was supported by the National Natural Science Foundation of China (No. 52205455), the Natural and Science Foundation of Fujian Province (No. 2021J01560), the Education and Scientific Research Foundation for Young Teachers in Fujian Province (No. JAT190006), and the Foreign Cooperation Project from Natural Science Foundation of Fujian Province of China (No. 2020I0028). The authors also thank Guangzhou Boxin Medical Technology Co. and Fujian Luochuang Medical Technology Co. for providing the relevant equipment support.

Author contributions Conceptualization: CHG and ZJZ; methodology: CHG, ZRH, YL, and LJC; writing—original draft: CHG and ZRH; writing—review & editing: CHG and ZJZ; supervision: ZJZ, LHL, and MCF; project administration: BWH. All authors have read and agreed to the published version of the manuscript.

Declarations

Conflict of interest The authors declare that they have no conflict of interest.

Ethical approval This study does not contain any studies with human or animal subjects performed by any of the authors.

References

1. Libby P, Ridker PM, Hansson GK (2011) Progress and challenges in translating the biology of atherosclerosis. Nature 473(7347):317–325. https://doi.org/10.1038/nature10146
2. Tabas I (2010) Macrophage death and defective inflammation resolution in atherosclerosis. Nat Rev Immunol 10(2):36–46. https://doi.org/10.1038/nri2675
3. Libby P, Ridker PM, Hansson GK (2012) Inflammation in atherosclerosis. J Assoc Phys India 32(9):2045–2051. https://doi.org/10.1161/ATVBAHA.108.179705
4. Hansson GK (2005) Inflammation, atherosclerosis, and coronary artery disease. N Engl J Med 352(16):1685–1695. https://doi.org/10.1056/NEJMra043430
5. Patel A, Irani FG, Pua U et al (2021) Randomized controlled trial comparing drug-coated balloon angioplasty versus conventional balloon angioplasty for treating below-the-knee arteries in critical limb ischemia: the SINGA-PACLI trial. Radiology 300(3):715–724. https://doi.org/10.1148/radiol.2021204294
6. Hasan MA, Murugan R (2012) Stenting versus aggressive medical therapy for intracranial arterial stenosis: more harm than good. Crit Care 16(3):310. https://doi.org/10.1186/cc11326
7. Ferri LA, Jabbour RJ, Giannini F et al (2016) Safety and efficacy of rotational atherectomy for the treatment of undilatable underexpanded stents implanted in calcific lesions. Catheter Cardiovasc Interv 90(2):E19–E24. https://doi.org/10.1002/ccd.26836
8. Tomey MI, Kini AS, Sharma SK (2014) Current status of rotational atherectomy. JACC Cardiovasc Interv 62(4):485–498. https://doi.org/10.1016/j.jcin.2013.12.196
9. Kusumoto H, Ishibuchi K, Hasegawa K et al (2022) Trans-coronary pacing via Rota wire prevents bradycardia during rotational atherectomy: a case report. Eur Heart J Case Rep 6(2):ytac013. https://doi.org/10.1093/ehjcr/ytac013

10. Solomonica A, Lavi S, Cui J et al (2020) Radial versus femoral approach for rotational atherectomy. Coron Artery Dis 31(4):393–395. https://doi.org/10.1097/MCA.0000000000000843
11. Ahn SS, Auth D, Marcus DR et al (1988) Removal of focal atheromatous lesions by angioscopically guided high-speed rotary atherectomy. J Vasc Surg 7(2):292–300
12. Widasmara S, Rohman MS, Martini H et al (2021) Case report: role of rotational atherectomy in complex PCI. Heart Sci J 2(3):35–40. https://doi.org/10.21776/ub.hsj.2021.002.03.7
13. Mori T, Sakakura K, Wada H et al (2016) Comparison of mid-term clinical outcomes between on-label and off-label use of rotational atherectomy. Heart Vessels 32(5):514–519. https://doi.org/10.1007/s00380-016-0899-6
14. Jinnouchi H, Sakakura K, Taniguchi Y et al (2022) Intravascular ultrasound-factors associated with slow flow following rotational atherectomy in heavily calcified coronary artery. Sci Rep 12(1):5674. https://doi.org/10.1038/s41598-022-09585-z
15. Levin TN, Carroll JD, Feldman T (2015) Bail-out stenting for flow limiting dissections after rotational atherectomy in complex coronary lesions. Cathet Cardiovasc Diagn 37(3):300–304. https://doi.org/10.1002/(SICI)1097-0304(199603)37:3%3c300::AID-CCD18%3e3.0.CO;2-L
16. Motwani JG, Raymond RE, Franco I et al (2000) Effectiveness of rotational atherectomy of right coronary artery ostial stenosis. Am J Cardiol 85(5):563–567. https://doi.org/10.1016/s0002-9149(99)00812-7
17. Sakakura K, Ako J, Wada H et al (2012) Beta-blocker use is not associated with slow flow during rotational atherectomy. J Invasive Cardiol 24(8):379–384
18. Matsuo H, Watanabe S, Watanabe T et al (2007) Prevention of no-reflow/slow-flow phenomenon during rotational atherectomy—a prospective randomized study comparing intracoronary continuous infusion of verapamil and nicorandil. Am Heart J 154(5):994.e1-994.e6. https://doi.org/10.1016/j.ahj.2007.07.036
19. Muschart X, Slimani A, Jamart J et al (2014) Mechanisms of periprocedural myocardial necrosis following Rotablator® and saphenous vein graft PCI. Exp Clin Cardiol 20(1):2579–2587
20. Tanaka Y, Saito S (2016) Successful retrieval of a firmly stuck rotablator burr by using a modified STAR technique. Catheter Cardiovasc Interv 87(4):749–756. https://doi.org/10.1002/ccd.26342
21. Sakakura K, Ako J, Momomura S (2011) Successful removal of an entrapped rotablation burr by extracting drive shaft sheath followed by balloon dilatation. Catheter Cardiovasc Interv 78(4):567–570. https://doi.org/10.1002/ccd.22957
22. Khalid N, Javed H, Shlofmitz E et al (2020) Adverse events and modes of failure related to rotational atherectomy system: the utility of the MAUDE database. Cardiovasc Revasc Med 27:57–62. https://doi.org/10.1016/j.carrev.2020.08.038
23. Nakao M, Tsuchiya K, Maeda W et al (2005) A rotating cutting tool to remove hard cemented deposits in heart blood vessels without damaging soft vessel walls. CIRP Ann Manuf Technol 54(1):37–40. https://doi.org/10.1016/S0007-8506(07)60044-4
24. Lee GY, Wie KH, Hong YS et al (2010) A study of tool pattern design for calcified-atherosclerotic-plaque removal robot. In: Proceedings of the 3rd IEEE RAS & EMBS International Conference on Biomedical Robotics and Biomechatronics, pp 582–587. https://doi.org/10.1109/BIOROB.2010.5627037
25. Lyu JJX, Wu X, Liu Y et al (2019) A miniature nickel-diamond electroplated wheel for grinding of the arterial calcified plaque. Procedia Manuf 34:222–227. https://doi.org/10.1016/j.promfg.2019.06.142
26. Mizutani T, Enomoto T, Satake U (2018) Surgical diamond wheels for minimally invasive surgery in bone resection under saline supply. Procedia CIRP 77:243–246. https://doi.org/10.1016/j.procir.2018.09.006
27. Luo Y, Chen L, Shih AJ (2019) Hollow notched K-wires for bone drilling with through-tool cooling. J Orthop Res 37(11):2297–2306. https://doi.org/10.1002/jor.24419
28. Liu Y, Belmont B, Wang Y et al (2017) Notched K-wire for low thermal damage bone drilling. Med Eng Phys 45:25–33. https://doi.org/10.1016/j.medengphy.2017.04.001
29. Wexler L, Brundage B, Crouse J et al (1996) Coronary artery calcification: pathophysiology, epidemiology, imaging methods, and clinical implications. A statement for health professionals from the American Heart Association. Circulation 94(5):1175–1192. https://doi.org/10.1161/01.cir.94.5.1175
30. Ebenstein DM, Coughlin D, Chapman J et al (2009) Nanomechanical properties of calcification, fibrous tissue, and hematoma from atherosclerotic plaques. J Biomed Mater Res A 91(4):1028–1037. https://doi.org/10.1002/jbm.a.32321
31. Zhu L, Zhao HP, Song YL et al (2006) Experimental investigation of the mechanical properties of Takin femoral cortical bone. J Tsinghua Univ Sci Technol 46(2):301–304 (in Chinese)
32. Freitas RA (1999) Nanomedicine, volume I: basic capabilities. Landes Bioscience, Georgetown
33. Ahn SS, Auth D, Marcus DR et al (1988) Removal of focal atheromatous lesions by angioscopically guided high-speed rotary atherectomy. Preliminary experimental observations. J Vasc Surg 7(2):292–300. https://doi.org/10.1016/10.1067/mva.1988.avs0070292